



Modelling and simulation of the operation of a calorimetric sensor for medical application

P. J. Rodríguez de Rivera^{1,2} · Mi. Rodríguez de Rivera¹ · F. Socorro¹ · M. Rodríguez de Rivera¹ · G. M. Callicó²

Received: 4 November 2019 / Accepted: 13 March 2020 / Published online: 27 March 2020
© Akadémiai Kiadó, Budapest, Hungary 2020

Abstract

A calorimetric sensor for medical application has been developed to measure surface and localize heat dissipations of human body. The instrument evaluates the heat flux transmitted by conduction, through a thermopile, between the human body surface and a programmed thermostat at a set temperature. In this work, a model with twelve transfer functions describing the operation of the sensor is exposed. This model relates the inputs to outputs of the system. Sensitivities, poles and zeros of each of the transfer functions are obtained with two independent experimental measurements and a numerical optimization method based on the adjustment of the experimental output curves with the ones calculated by the model. The model simulates the operation of the sensor, determines its operating limits and assesses the flow of heat between human skin and the thermostat sensor. The proposed method is applicable to any non-differential calorimeter.

Keywords Direct calorimetry · Heat conduction calorimeters · Medical calorimetry · Non-differential calorimetry

Introduction

Modelling a calorimeter is to establish mathematical relationships between the variables involved in the energy process under study and the variables measured and controlled by the instrument [1–4]. These mathematical relationships allow accurately determining the power and/or the heat energy developed in this process and also to study the related magnitudes, such as the heat capacity of the sample under study. The modelling also allows to determine the operating

limits of the instrument and to study the effect of the actions that make it possible to start the process under study [5–7]. In addition, depending on the model chosen, the modelling helps relating the static and the dynamic operating of the calorimeter with its own design. In this work, a model of the operation of a calorimetric sensor specially designed to measure the heat power dissipated by a surface and localized area of the human body is exposed.

This sensor is non-differential, and the measured heat power is transferred by conduction from the surface of the human body to a thermostat located inside the calorimetric sensor. Therefore, we can include this instrument within the group of non-differential calorimeters [8]. Besides, this instrument is outside the standards of calorimetry [9, 10] as the studied process is not within the calorimeter and consequently is not isolated from external disturbances.

The information obtained with this sensor can complement other studies of human surface temperature measured by thermography [11, 12]. In addition, this calorimetric sensor can be used to study several pathologies that can currently be monitored with thermography [13–20].

The first prototype constructed of this calorimetric sensor had a detection surface of $6 \times 6 \text{ cm}^2$ [21–24]. The second built sensor is similar but smaller in size, with a detection surface of $2 \times 2 \text{ cm}^2$ [25–27]. The advantages of the second prototype over the first one are: (1) easier handling for

✉ M. Rodríguez de Rivera
manuel.riguezderivera@ulpgc.com

P. J. Rodríguez de Rivera
pedrojrdrs@gmail.com

Mi. Rodríguez de Rivera
miriam.mrdrs@gmail.com

F. Socorro
fabiola.socorro@ulpgc.com

G. M. Callicó
gustavo@iuma.ulpgc.es

¹ Departamento de Física, Universidad de Las Palmas de Gran Canaria, 35017 Las Palmas, Spain

² Instituto Universitario de Microelectrónica Aplicada (IUMA), Universidad de Las Palmas de Gran Canaria, 35017 Las Palmas, Spain

application to different parts of the human body, (2) greater sensitivity and (3) faster dynamic response. This work focuses on the second sensor of which two prototypes have been constructed allowing cross-measurements [28]. The development of this work begins with a description of the experimental system and the measured and controlled variables. Next, the model and identification results are presented. Finally, several simulations of the calorimeter operations are shown. From these simulations, it is possible to obtain useful information for the design of experiments, such as an estimation of the thermal working conditions in terms of thermostat temperatures and measurable powers for each room temperature.

Experimental system and measurement method

The sensor has a measurement area of $2 \times 2 \text{ cm}^2$. Figure 1 presents a scheme of the sensor's parts and its application on the skin. A measurement thermopile (part two in Fig. 1) provides the calorimetric signal, related to the heat flux between the measurement plate (part one in Fig. 1) and the thermostat (part three in Fig. 1). This heat flux is the one that pass across the thermopile, indicated by the red arrows in Fig. 1. Thermal insulation (part seven in Fig. 1) reduces oscillations caused by the environment. The thermostat can control the temperature with a resolution of 5 mK. The thermostat's temperature controller is a proportional integrative derivative controller (PID) [29–32].

In order to perform calibrations and ensure a good baseline, a calibration base (Fig. 2) is necessary. For the sensor operation, it is also required a data acquisition system and one power supply for each sensor. The two sensors available operate with a sampling period of 1 s. All these elements are described on detail in previous works [25, 26].

Calibration measurements are all made with the sensor located on its calibration base. The measurements with the sensor consist of its application on the human body surface. Before and after the sensor's application, the device is placed on the calibration base to ensure a good baseline. Usually, the measurements take 15 min: 5 min in calibration base (initial baseline), 5 min in human body and 5 min in calibration base (final baseline) [28].

Operating model and identification

The model considered has four inputs and three outputs. The two first inputs are the power generated by the human body that passes across the sensor, u_1 , and the power dissipated in the thermostat, u_2 . When measured on the skin of the human body $u_1 = W_{\text{body}}$, but when the sensor is placed on the calibration base, the power u_1 is the power dissipated in the resistance used to calibrate the sensor. The other two inputs are the voltage applied to the cooling thermopile, $u_3 = V_{\text{peltier}}$, and the power dissipated in the cooling thermopile, represented by $u_4 = V_{\text{peltier}}^2$. The operation of the cooling thermopile is nonlinear. This is experimentally checked for both voltage (0–2 V) and intensity (0–0.34 A) values used. For this reason, we consider two inputs for the thermopile supply: the voltage that produces the cooling effect and the squared voltage that is proportional to the power dissipated by Joule effect. The outputs are the following ones: the temperature of the calibration base y_1 , the sensor's thermostat temperature y_2 and the calorimetric signal y_3 provided by the measuring thermopile. The model, which consists of twelve transfer functions TF_{ij} that relate inputs to outputs, allows us to simulate the operation of the sensor. In Laplace domain, the model is defined by Eq. 1.

Fig. 1 Scheme of the calorimetric sensor and its application on the skin. (1) Aluminium plate, (2) measurement thermopile by Seebeck effect, (3) thermostat containing RTD sensor and heater resistor, (4) cooling thermopile by Peltier effect, (5) aluminium heat sink, (6) fan and (7) thermal insulation

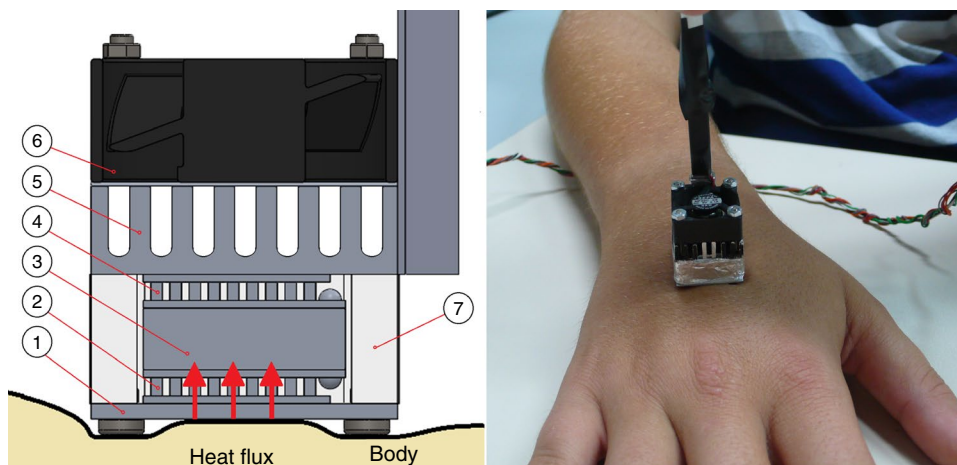
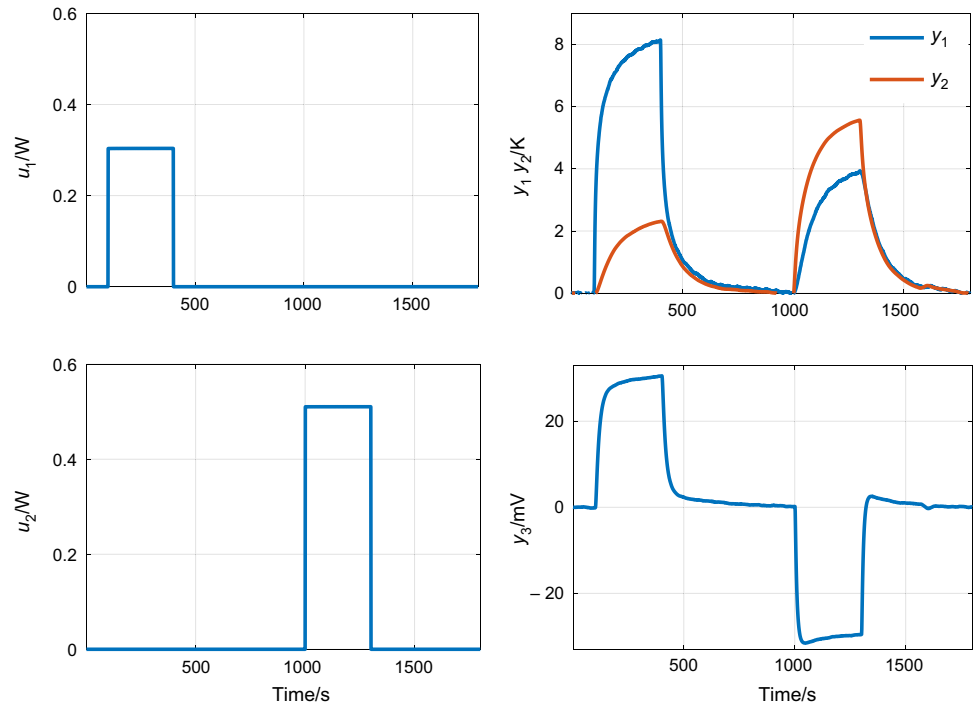


Fig. 2 Calibration measurement 1 with corrected baselines (sensor 1). The input powers are u_1 and u_2 that are dissipated in the base and thermostat, respectively. The outputs are the temperatures of the base (y_1) and the thermostat (y_2), and the calorimetric signal (y_3)



$$Y_i(s) = \sum_{j=1}^4 TF_{ij}(s) \cdot U_j(s) \quad i = 1, 3 \tag{1}$$

Given the signal-to-noise ratio of the experimental curves, two poles in each TF_{ij} are sufficient to reconstruct the output signals. This determines the shape of each TF_{ij} , which is indicated in Eq. 2.

$$TF_{ij}(s) = \frac{K_{ij} \cdot (1 + s \cdot \tau_{ij}^*)}{(1 + s \cdot \tau_{1ij}) \cdot (1 + s \cdot \tau_{2ij})} \tag{2}$$

where K_{ij} is the sensitivity (stationary response to an input Heaviside), τ_{1ij} and τ_{2ij} are the time constants (opposite of the inverses of the poles) and τ_{ij}^* is the opposite to the inverse of the zero.

Two measures are designed for identification. The first one consists in dissipating 300 mW (u_1) in the calibration base for 300 s. Then, spaced 600 s in time, a power of 500 mW (u_2) on the thermostat is dissipated during 300 s (Fig. 2). This measure allows determining the relationship between the outputs (y_1 , y_2 and y_3) and the inputs (u_1 and u_2). The second measure is to program variations on the voltage (u_3) of the cooling thermopile by successively applying different voltages: 0.0, 0.4, 0.8, 1.2, 1.6 and 2.0 V for 600 s in each voltage (Fig. 3). This second measurement determines the relationship between inputs u_3 and $u_4 = u_3^2$ and outputs (y_1 , y_2 and y_3).

The identification process is as follows. We use an iterative process based on Nelder–Mead algorithm [33–35] to

determine the sensitivity, poles and zeros of each TF_{ij} . This algorithm minimizes the mean squared error (Eq. 3) between the signals calculated with the model (signals_{Cal.} in Figs. 4, 5) and the experimental ones (signals_{Exp.} in Figs. 4, 5).

$$\epsilon = \frac{1}{N} \sqrt{\sum_{i=1}^N (y_{exp}[i] - y_{cal}[i])^2} \tag{3}$$

First, the parameters of the two TFs that relate the output y_1 to the inputs u_1 and u_2 (TF_{11} and TF_{12}) are identified. According to the RC modelling of the calorimeters [1–4], we consider that the time constants of these two TFs are the same. Sensitivities and zeros are different for each TF. The procedure is the same to determine the parameters of the TFs that relate the outputs y_2 and y_3 to the inputs u_1 and u_2 (TF_{21} , TF_{22} , TF_{31} and TF_{32}). Table 1 shows the results obtained, and Fig. 4 shows the fit between experimental and calculated curves.

The same procedure is applied to determine the parameters of the TF that relate the outputs y_1 , y_2 and y_3 to the inputs u_3 and u_4 . Table 2 shows the results obtained, and Fig. 5 shows the fit between experimental and calculated curves.

The RC modelling of calorimeters by heat conduction implies the decomposition of the device in as many domains as dissipation and detection elements exist. The number of domains determines the number of poles. These poles are the same for all TFs that relate the inputs to outputs. On the other hand, the experimental signal/noise

Fig. 3 Calibration measurement 2 with corrected baselines (sensor 1). The input signals are the voltage applied to the cooling thermopile (u_3) and its squared value ($u_4 = u_3^2$). The outputs are the temperatures of the base (y_1) and the thermostat (y_2) and the calorimetric signal (y_3)

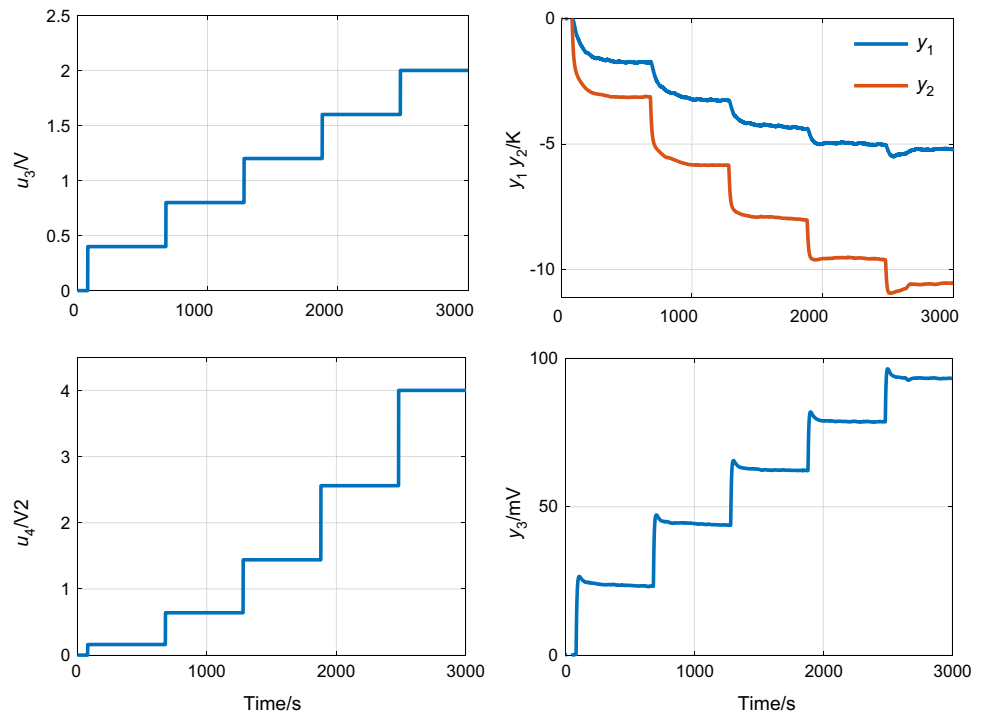
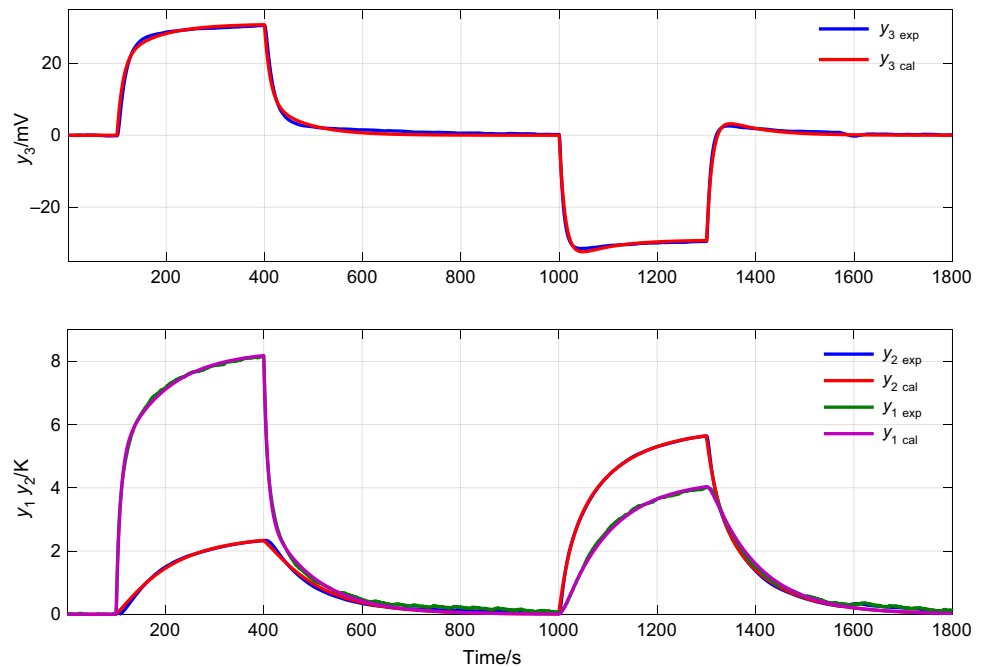


Fig. 4 Adjustment of experimental outputs (y_{exp}) and calculated (y_{cal}) by the model. The input powers are the dissipated powers at the base and thermostat, respectively (u_1 and u_2). The outputs are the temperatures of the base (y_1) and the thermostat (y_2) and the calorimetric signal (y_3). Measurement corresponding to Fig. 2



ratio does not allow the identification of TFs of more than two poles. For each output y_i , the TFs related to u_1 and u_2 (TF_{i1} and TF_{i2}) have common poles. However, the TFs related to u_3 and u_4 involve the cooling thermopile and, therefore, TF_{i3} and TF_{i4} have identical poles, but different from those of TF_{i1} and TF_{i2} .

Simulations

Temperature control

The simulations from this model are very useful for checking the proper functioning of the thermostat temperature

Fig. 5 Adjustment of experimental outputs (y_{exp}) and calculated (y_{cal}) by the model. The input signals are the voltage applied to the cooling thermopile (u_3) and its squared value ($u_4 = u_3^2$). The outputs are the temperatures of the base (y_1) and the thermostat (y_2) and the calorimetric signal (y_3). Measurement corresponding to Fig. 3

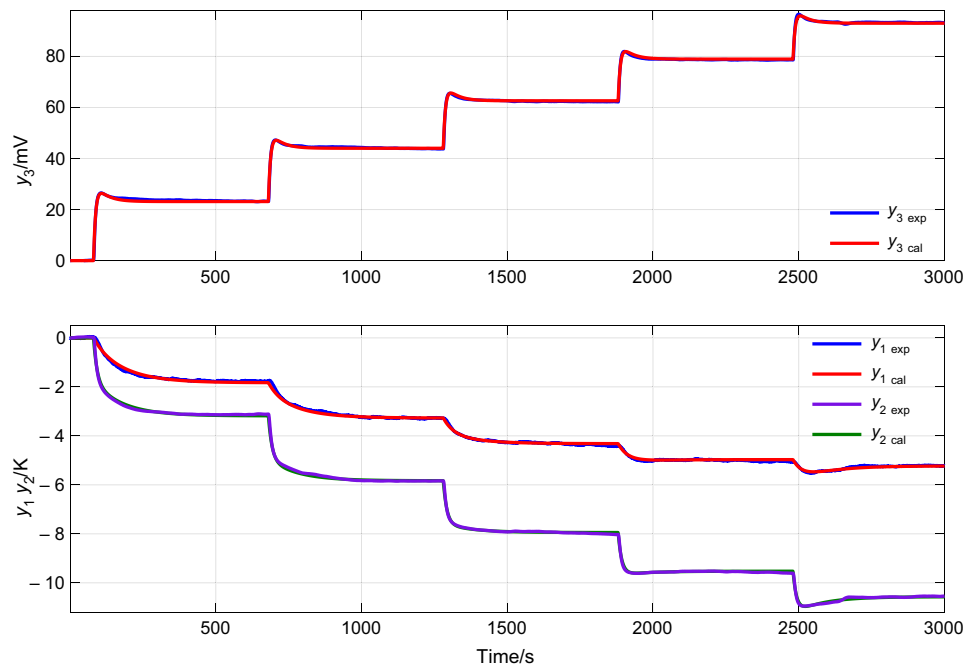


Table 1 TF parameters that relate the outputs y_1, y_2 and y_3 to the inputs u_1 and u_2

Inputs: u_1 (base joule power), u_2 (thermostat joule power)
 Outputs: $y_1 = T_{base}/K, y_2 = T_{thermostat}/K, y_3 = Y_{calorimetric}/mV$

Outputs y_i	K_{i1}	K_{i2}	$\tau_{i11} = \tau_{1i2}/s$	$\tau_{2i1} = \tau_{2i2}/s$	τ_{i1}^*/s	τ_{i2}^*/s	Error (Eq. 3)
Sensor 1							
y_1	27.47 K W ⁻¹	8.33 K W ⁻¹	98.0	8.5	61.3	0.0	2.0 mK
y_2	8.18 K W ⁻¹	11.46 K W ⁻¹	102.9	23.1	15.0	50.5	1.3 mK
y_3	101.86 mV W ⁻¹	-57.07 mV W ⁻¹	74.9	11.8	54.7	91.0	14.7 μ V
Sensor 2							
y_1	36.19 K W ⁻¹	7.21 K W ⁻¹	108.3	8.5	77.2	1.0	2.0 mK
y_2	8.53 K W ⁻¹	9.86 K W ⁻¹	105.6	31.8	26.0	55.0	1.1 mK
y_3	121.38 mV W ⁻¹	-43.53 mV W ⁻¹	169.3	15.1	147.6	193.3	13.4 μ V

$$Y_1(s) = K_{i1} \frac{(1+s\tau_{i1}^*)}{(1+s\tau_{i11})(1+s\tau_{2i1})} U_1(s) + K_{i2} \frac{(1+s\tau_{i2}^*)}{(1+s\tau_{i12})(1+s\tau_{2i2})} U_2(s)$$

Table 2 TF parameters that relate the outputs y_1, y_2 and y_3 to the inputs u_3 and u_4

Inputs: $u_3 = V_{peltier}, u_4 = V_{peltier}^2$ ($V_{peltier}$: cooling thermopile voltage)
 Outputs: $y_1 = T_{base}/K, y_2 = T_{thermostat}/K, y_3 = Y_{calorimetric}/mV$

Outputs y_i	K_{i3}	K_{i4}	$\tau_{i13} = \tau_{1i4}/s$	$\tau_{2i3} = \tau_{2i4}/s$	τ_{i3}^*/s	τ_{i4}^*/s	Error (Eq. 3)
Sensor 1							
y_1	-5.07 K V ⁻¹	1.23 K V ⁻²	105.5	33.1	37.9	0.0	0.9 mK
y_2	-8.18 K V ⁻¹	1.67 K V ⁻²	98.9	12.2	57.0	14.0	0.7 mK
y_3	60.71 mV V ⁻¹	-7.10 mV V ⁻²	36.6	7.5	47.0	40.7	7.2 μ V
Sensor 2							
y_1	-5.31 K V ⁻¹	1.12 K V ⁻²	92.6	32.1	42.3	7.8	0.8 mK
y_2	-9.48 K V ⁻¹	1.65 K V ⁻²	73.6	13.8	48.6	20.6	1.2 mK
y_3	66.22 mV V ⁻¹	-6.83 mV V ⁻²	59.8	5.8	68.6	62.6	5.7 μ V

$$Y_1(s) = K_{i3} \frac{(1+s\tau_{i3}^*)}{(1+s\tau_{i13})(1+s\tau_{2i3})} U_3(s) + K_{i4} \frac{(1+s\tau_{i4}^*)}{(1+s\tau_{i14})(1+s\tau_{2i4})} U_4(s)$$

control and adjusting its parameters. The controller chosen is a PID controller (proportional, integrative and derivative) whose transfer function is given by Eq. 4.

$$G_{PID}(s) = \left(k_p + \frac{k_i}{s} + k_d s \right) \tag{4}$$

Initially, the parameters k_p , k_i and k_d are determined by Ziegler–Nichols tuning rules [29–32]. Then, by means of successive simulations, these values are adjusted until the desired specifications are obtained. Figure 6 shows a scheme

of the control loop in which a limiter of the power dissipated in the thermostat (from 0 to 2 W) is included.

It has been verified that the adjusted control parameters are maintained as long as the limits of the thermostat power and the sampling period ($\Delta t = 1$ s) do not change; otherwise, these parameters must be readjusted again. An important advantage of the identification of the controller by means of this model is the saving of time involved. Although a new system identification is necessary, the total time required to calculate the parameters of the controller is less than the one that is necessary experimentally.

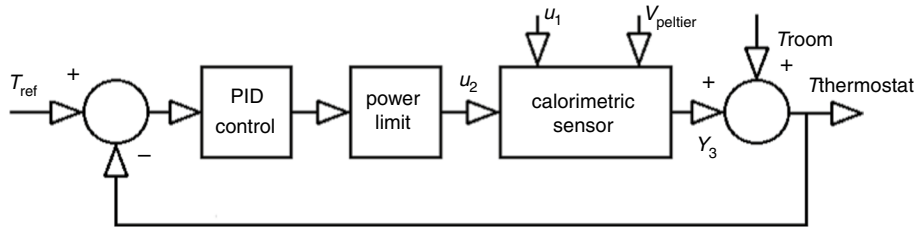


Fig. 6 Scheme of the thermostat temperature control loop. T_{ref} is the programmed temperature of the thermostat. u_2 is the power dissipated in the thermostat. u_1 is the power to be measured (from the human body). $V_{peltier}$ is the voltage of the cooling thermopile. T_{room} is room temperature

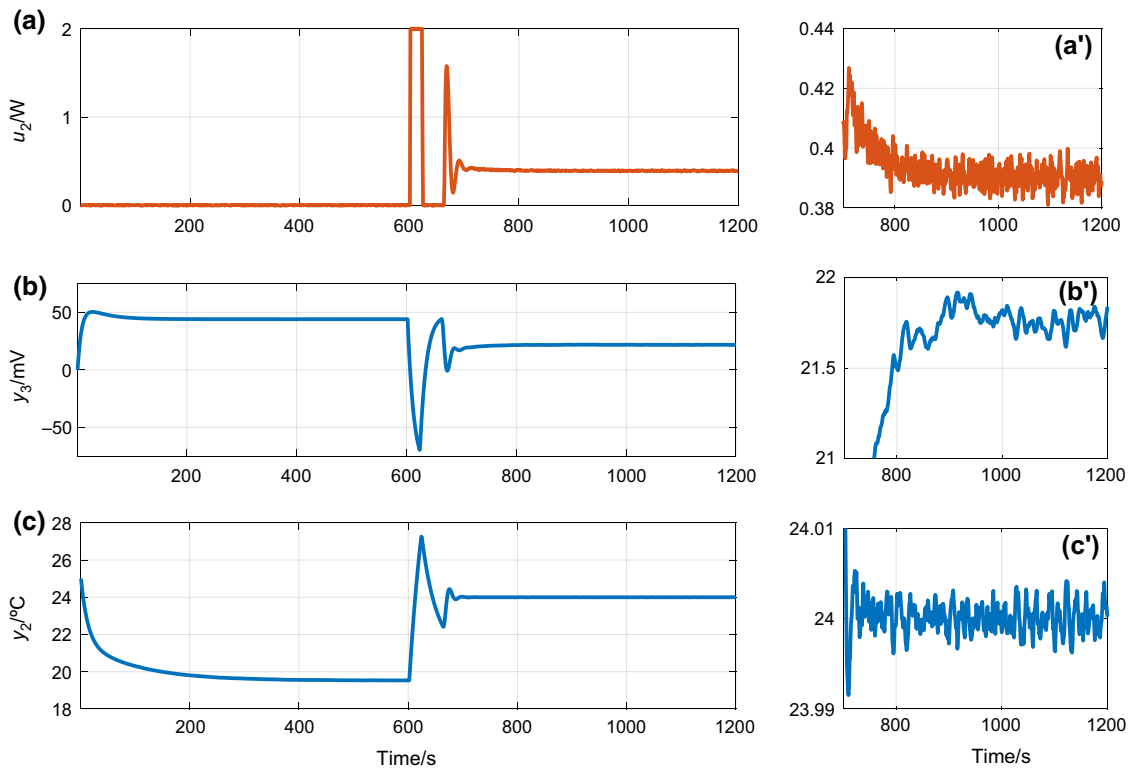


Fig. 7 Simulation of the operation of the thermostat temperature control (the control starts at $t = 600$ s). **a** Power dissipated in the thermostat. **b** Calorimetric signal. **c** Thermostat temperature. **a'**, **b'**, **c'** repre-

sent a zoom of the final part of curves **a**, **b** and **c**, respectively (from $t = 700$ s to $t = 1200$ s)

Figure 7 shows the operation of the temperature control for two consecutive periods of time. In the first period (600 s), a constant voltage of 0.8 V is applied to the cooling thermopile for a room temperature of 25 °C and the thermostat temperature drops to a value of 19.53 °C. The PID controller is then started to reach a thermostat temperature of 24 °C. This simulation has included a noise of ± 10 mW in the power, which produces a noise of ± 0.15 mV in the calorimetric signal and ± 4 mK in the thermostat temperature. These values are very similar to the experimental ones. The steady state of the thermostat temperature is reached at 150 s. However, the calorimetric signal reaches the stationary at 250 s. This implies that 300 s are enough to reach steady state. The values of the parameters used in the PID controller (Eq. 4) are the following: $k_p=0.96$ W K⁻¹; $k_i=0.32$ W K⁻¹ s⁻¹; $k_d=0.72$ W K⁻¹ s.

Operation range

The controller is able to keep the thermostat temperature constant independent of the voltage applied to the cooling thermopile. However, it is necessary to correctly adjust this value to prevent the sensor saturation. According to the proposed modelling, the thermostat temperature is given by Eq. 5.

$$T_{\text{Thermostat}} = \frac{T_{\text{room}}}{s} + Y_2(s) = \frac{T_{\text{room}}}{s} + \sum_{j=1}^4 \text{TF}_{2j}(s) \cdot U_j(s) \quad (5)$$

In steady state and for sensor 1, Eq. 5 has the following form:

$$T_{\text{Thermostat}} = \frac{T_{\text{room}}}{s} + 8.18W_{\text{body}} + 11.46W_{\text{Thermostat}} - 8.18V_{\text{peltier}} + 1.67V_{\text{peltier}}^2 \quad (6)$$

T_{room} being the room temperature, W_{body} is the power that passes through the sensor that comes from the human body

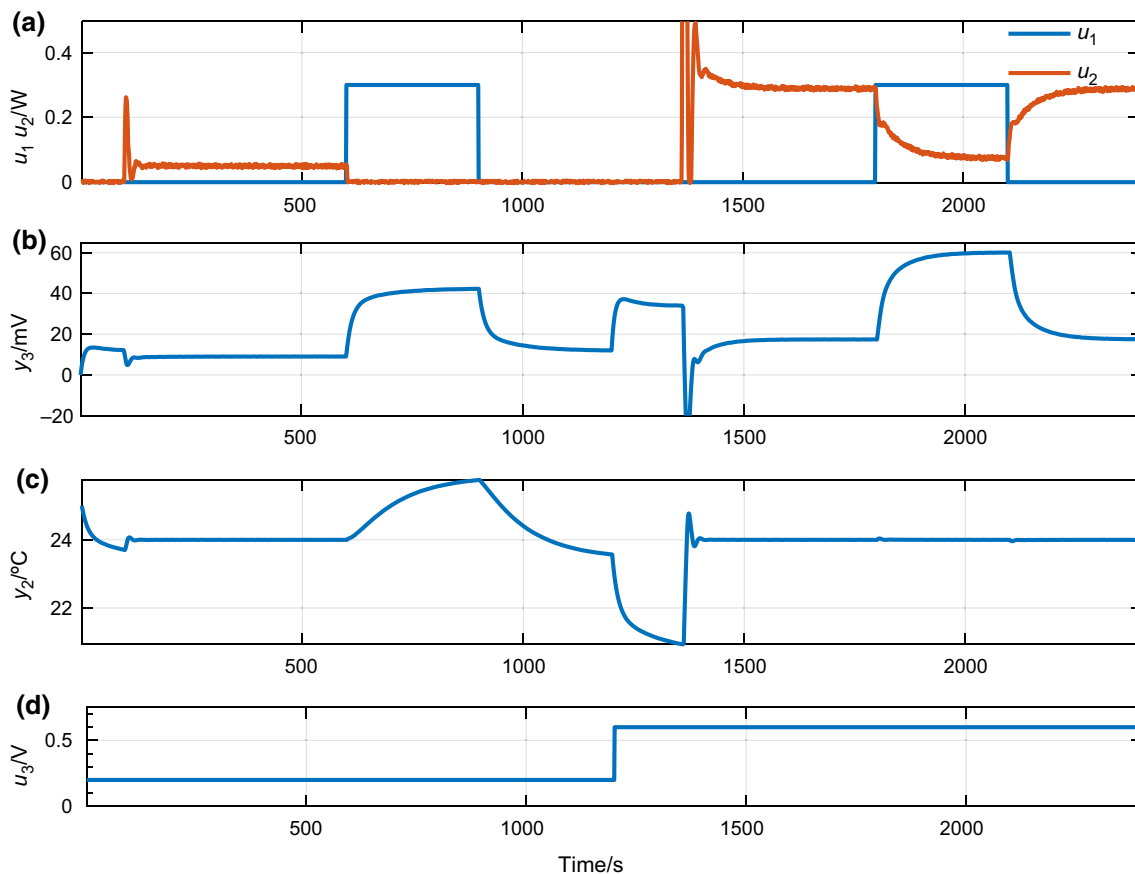


Fig. 8 Simulation of the operation of the thermostat temperature control (curve c) when a power of 300 mW for 300 s crosses the sensor (curve blue in a), for cases of a voltage in the cooling thermopile of

0.2 V and 0.6 V (curve d). Power dissipated in the thermostat (red curve in a). Calorimetric signal, (curve b)

Table 3 Power dissipated in the thermostat as a function of the thermostat temperature ($T_{\text{thermostat}}$), the room temperature (T_{room}) and the voltage applied to the cooling thermopile (V_{peltier})

$T_{\text{room}}/^\circ\text{C}$	$V_{\text{peltier}}/\text{V}$	Thermostat temperature			
		24 °C	28 °C	32 °C	36 °C
18	0.0	0.267 W	0.699 W	1.131 W	1.564 W
20	0.4	0.354 W	0.787 W	1.219 W	1.651 W
22	0.8	0.395 W	0.828 W	1.260 W	1.692 W
24	1.2	0.390 W	0.822 W	1.254 W	1.687 W
26	1.6	0.338 W	0.770 W	1.202 W	1.635 W
28	2.0	0.239 W	0.671 W	1.103 W	1.536 W

or the calibration base and V_{peltier} the voltage applied to the cooling thermopile. Equations 5 and 6 allow to determine the voltage to be applied to the cooling thermopile to be able to correctly program the thermostat temperature taking into account the maximum value of $W_{\text{Thermostat}}$ (2 W) and the value of W_{body} .

As an example, Fig. 8 shows the simulation of the operation of the sensor for a room temperature of $T_{\text{room}} = 25^\circ\text{C}$ in two different situations.

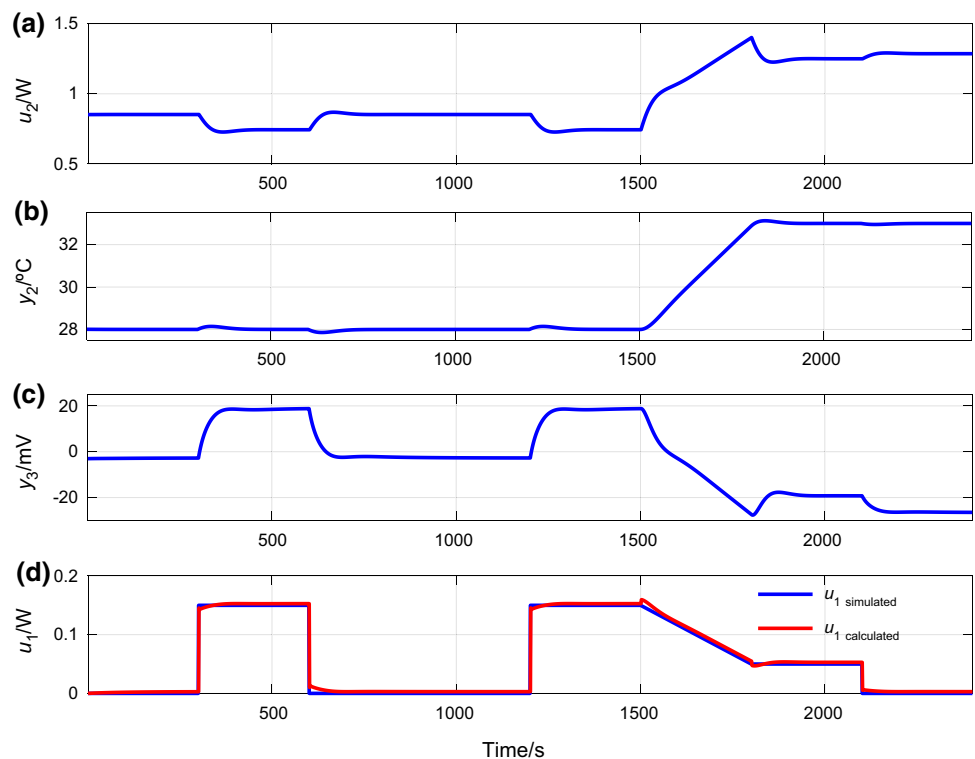
- In the first case, the voltage in the cooling thermopile is 0.2 V. Consequently, when a power of 300 mW passes through the sensor (blue curve of Fig. 8a), the thermostat temperature control is lost.

- In the second case, simulated below, when the cooling thermopile voltage is increased to 0.6 V, the thermostat temperature control keeps the programmed 24°C value.

Table 3 shows the recommended voltage values to be applied to the cooling thermopile according to the thermostat temperature. The power dissipated in the thermostat is also indicated depending on the temperature of the thermostat. In the calculation, it has been considered that the W_{body} power varies linearly from 360 mW for a thermostat temperature of 24°C to 10 mW for a thermostat temperature of 36°C . This hypothesis is based on the order of magnitude of the experimental measurements obtained with this sensor, in which it is verified that the surface heat flux of the human body depends directly on the temperature of the thermostat. The higher the temperature of the thermostat, the lower the heat flow between the surface of the human body and the thermostat [28].

These simulations manifest the importance of the correct programming of the cooling voltage. These relationships (Eqs. 5, 6) allow the sensor to operate in any reasonable environment with room temperatures between 18 and 28°C . This is of great importance, since it facilitates its use in installations where the surrounding temperature cannot be controlled.

Fig. 9 Simulation of sensor operation. **a** Power dissipated in the thermostat. **b** Thermostat temperature. **c** Calorimetric signal. **d** Simulated power (blue curve) and power calculated with Eq. 7 (red curve)



Estimation of heat flow dissipated by the human body

The main objective of this calorimetric sensor is to determine the human heat flux when applied to the skin of the human body. Two dissipations in the human body are simulated (Fig. 9): the first one with $W_{\text{body}} = 150$ mW for a constant thermostat temperature of 28 °C. ($T_{\text{room}} = 24$ °C, $V_{\text{peltier}} = 0.8$ V). The second dissipation corresponds to a linear variation of the thermostat temperature, where the dissipation is $W_{\text{body}} = 150$ mW for $T_{\text{thermostat}} = 28$ °C and $W_{\text{body}} = 50$ mW for $T_{\text{thermostat}} = 33$ °C ($T_{\text{room}} = 24$ °C, $V_{\text{peltier}} = 0.8$ V). Being the voltage applied to the cooling thermopile constant throughout the whole measurement (which is usual and recommended), the power is calculated with Eq. 7.

$$U_{\text{cal}}(s) = \frac{Y_3(s) \cdot (1 + s\tau_1) \cdot (1 + s\tau_2) - K_{32} \cdot (1 + s\tau_{32}^*) \cdot U_2(s)}{K_{31} \cdot (1 + s\tau_{31}^*)}$$

$$\tau_1 = \tau_{131} = \tau_{132}; \quad \tau_2 = \tau_{231} = \tau_{232} \quad (7)$$

Being $y_3(t)$, the calorimetric signal and $u_2(t)$ the power dissipated by the thermostat. Table 1 previously shown indicates the values of the TF parameters that relate y_3 to the powers u_1 and u_2 (K_{31} , K_{32} , τ_{131} , τ_{231} , τ_{31}^* , τ_{32}^*).

Figure 9 shows the curves corresponding to these two simulations. The good adjustment of the deconvolution obtained with Eq. 7 (red curve in Fig. 9d) with the simulation (blue curve in Fig. 9d) can be observed. With this simulation, we check the ability of the model to simulate measurements on the surface of the human body with different temperatures of the thermostat, for simple measurements (with the thermostat at constant temperature) and complex ones (with a programmed variation of the thermostat, in this case linear variation).

Conclusions

A method of calibration for the calorimetric sensor is proposed, consisting of the identification of twelve transfer functions that describe the operation of the sensor and that relate the inputs to the outputs of the system. With two independent experimental measurements and a numerical method of optimization, based on the adjustment of the experimental output curves with those calculated by the model, the sensitivities, poles and zeros of each of the transfer functions are obtained.

While the model is still under development and it presents some limitations, it is currently of interest for the following applications:

- The simulations performed with this model are an ideal complement that greatly reduces the time required for the identification of the PID temperature controller. The Ziegler Nichols method requires several experiments that can be simulated using the exposed model in a much shorter time. The controller set by the model works as well as the experimental one.
- This model allows simulating the operation of the thermostat and the cooling system, which allows estimating the operating range of the device based on the measurement conditions. In our case, the sensor is able to operate for room temperatures between 18 and 28 °C and for thermostat temperatures between 24 and 36 °C.
- The purpose of this instrument is the determination of the heat flux transmitted by conduction between the surface of the human body and the sensor thermostat. The modelling allows evaluating such power for different constant temperatures of the thermostat, even for cases of linear variation of the thermostat temperature.
- On the other hand, the proposed method is applicable to any heat conduction calorimeter. This method is being used for experimental design.

Funding This work was completed while Pedro Jesús Rodríguez de Rivera was beneficiary of a pre-doctoral grant given by the “Ministerio de Ciencia, Innovación y Universidades (Spain)” and the “Agencia Canaria de Investigación, Innovación y Sociedad de la Información del Gobierno de Canarias (Spain)”.

References

1. Isalgué A, Ortin J, Torra V, Viñals J. Heat flux calorimeters: dynamical model localized time constants. *An Fis.* 1980;76:192–6.
2. Socorro F, de Rivera MR, Jesús C. A thermal model of a flow calorimeter. *J Therm Anal Calorim.* 2001;64:357–66.
3. Socorro F, de la Nuez I, Rodríguez de Rivera M. Calibration of isothermal heat conduction calorimeters: case of flow calorimeters. *Measurement.* 2003;33:241–50.
4. Kirchner R, de Rivera MR, Seidel JM, Torra V. Identification of micro-scale calorimetric devices. Part VI. An approach by RC-representative model to improvements in TAM microcalorimeters. *J Therm Anal Calorim.* 2005;82:179–84.
5. Rodríguez de Rivera M, Socorro F. Flow microcalorimetry and thermokinetics of liquid mixtures. *J Therm Anal Calorim.* 2007;87:591–4.
6. Socorro F, Rodríguez de Rivera M. Modellization of the mixture dissipation in a flow microcalorimeter. *J Therm Anal Calorim.* 2007;88:741–4.
7. Jesús C, Socorro F, Rodríguez de Rivera M. New approach to Tian's equation applied to heat conduction and liquid injection calorimeters. *J Therm Anal Calorim.* 2012;110:1523–32.
8. Hansen LD. Toward a standard nomenclature for calorimetry. *Thermochim Acta.* 2001;371:19–22.

9. Wendlandt WW. *Thermal methods of analysis*. New York: Wiley; 1974.
10. Brown ME, editor. *Handbook of thermal analysis and calorimetry: principles and practice*, vol. 1. Amsterdam: Elsevier; 1998.
11. Lahiri BB, Bagavathiaappan S, Jayakumar T, Philip J. Medical applications of infrared thermography: a review. *Infrared Phys Technol*. 2012;55:221–35.
12. Livingston S, Nolan R, Frim J, Reed L, Limmer R. A thermographic study of the effect of body composition and ambient temperature on the accuracy of mean skin temperature calculations. *Eur J Appl Physiol Occup Physiol*. 1987;56:120–5.
13. Haidar SG, Charity RM, Bassi RS, Nicolai P, Singh BK. Knee skin temperature following uncomplicated total knee replacement. *Knee*. 2006;13:422–6.
14. Mehra A, Langkamer VG, Day A, Harris S, Spencer RF. Creative protein and skin temperature post total knee replacement. *Knee*. 2005;12:297–300.
15. Rajapakse C, Grennan DM, Jones C, Wilkinson L, Jayson M. Thermography in the assessment of peripheral joint inflammation—a re-evaluation. *Rheumatol Rehabil*. 1981;20:81–7.
16. Denoble AE, Hall N, Pieper CF, Kraus VB. Patellar skin surface temperature by thermography reflects knee osteoarthritis severity. *Clin Med Insights Arthritis Musculosketet Disord*. 2010;3:69–75.
17. Rokita E, Rok T, Taton G. Application of thermography for the assessment of allergen-induced skin reactions. *Med Phys*. 2011;38:765–72.
18. Vecchio PC, Adebajo AO, Chard MD, Thomas PP, Hazleman BL. Thermography of frozen sholder and rotator cuff tendinitis. *Clin Rheumatol*. 1992;11:382–4.
19. Miyakoshi N, Itoi E, Sato K, Suzuki K, Matsuura H. Skin temperature of the shoulder: circadian rhythms in normal and pathologic shoulders. *J Shoulder Elb Surg*. 1998;7:625–8.
20. Godoy SE, Hayat MM, Ramirez DA, Myers SA, Padilla RS, Krishna S. Detection theory for accurate and non-invasive skin cancer diagnosis using dynamic thermal imaging. *Biomed Opt Express*. 2017;8(4):2301–23.
21. Socorro F, Rodríguez de Rivera M. Development of a calorimetric sensor for medical application. Part I—operating model. *J Therm Anal Calorim*. 2010;99:799–802.
22. Jesús C, Socorro F, Rodríguez de Rivera M. Development of a calorimetric sensor for medical application. Part II. Identification and simulation. *J Therm Anal Calorim*. 2013;113:1003–7.
23. Jesús C, Socorro F, Rodríguez de Rivera M. Development of a calorimetric sensor for medical application. Part III. Operating methods and applications. *J Therm Anal Calorim*. 2013;113:1009–13.
24. Jesús C, Socorro F, Rodríguez de Rivera HJ, Rodríguez de Rivera M. Development of a calorimetric sensor for medical application. Part IV. Deconvolution of the calorimetric signal. *J Therm Anal Calorim*. 2014;116:151–5.
25. Socorro F, Rodríguez de Rivera PJ, Rodríguez de Rivera M. Calorimetric minisensor for the localized measurement of surface heat dissipated from the human body. *Sensors*. 2016;16:1864.
26. Socorro F, Rodríguez de Rivera PJ, Rodríguez de Rivera Mi, Rodríguez de Rivera M. Mathematical model for localised and surface heat flux of the human body obtained from measurements performed with a calorimetry minisensor. *Sensors*. 2017;17:2749.
27. Rodríguez de Rivera PJ, Rodríguez de Rivera Mi, Socorro F, Rodríguez de Rivera M. Method for transient heat flux determination in human body surface using a direct calorimetry sensor. *Measurement*. 2019;139:1–9.
28. Rodríguez de Rivera PJ, Rodríguez de Rivera Mi, Socorro F, Rodríguez de Rivera M. Measurement of human body surface heat flux using a calorimetric sensor. *J Therm Biol*. 2019;81:178–84.
29. Ogata K. *Modern control engineering*. Upper Saddle River: Prentice Hall; 2010.
30. Åström KJ, Hägglund T. *Advanced PID control*. Durham: Research Triangle Park, Instrumentation, Systems, and Automation Society; 2006.
31. Ziegler JG, Nichols NB. Optimum settings for automatic controllers. *ASME Trans*. 1942;64:759–68.
32. Ziegler JG, Nichols NB. Process lags in automatic control circuits. *ASME Trans*. 1943;65:433–44.
33. Lagarias JC, Reeds JA, Wright MH, Wright PE. Convergence properties of the Nelder–Mead simplex method in low dimensions. *SIAM J Optim*. 1998;9(1):112–47.
34. Nelder JA, Mead C. A simplex method for function minimization. *Comput J*. 1965;7:308–13.
35. *Optimization Toolbox™ User's Guide*, 5th printing; Revised for Version 3.0 (Release 14); The MathWorks, Inc.: Natic, MA, USA, June 2004.

Publisher's Note Springer Nature remains neutral with regard to jurisdictional claims in published maps and institutional affiliations.